Determining the aluminium occupancy on the active T-sites in zeolites using X-ray standing waves

JEROEN A. VAN BOKHOVEN[1]*, TIEN-LIN LEE[2]*†, MICHAEL DRAKOPOULOS[3], CARLO LAMBERTI[4], SEBASTIAN THIEß[2,5] AND JÖRG ZEGENHAGEN[2]

[1]ETH Zurich, Institute for Chemical and Bioengineering, HCI E127, 8093 Zurich, Switzerland
[2]European Synchrotron Radiation Facility, BP 220, F-38043 Grenoble Cedex 9, France
[3]Diamond Light Source Ltd, Harwell Science and Innovation Campus, Didcot OX11 0DE, UK
[4]Centre of Excellence NIS- Dipartimento di Chimica I.F.M., Università di Torino, Via P. Giuria 7, I-10125 Torino, Italy
[5]University Hamburg, Institut für Experimentalphysik, Luruper Chaussee 149, D-22761 Hamburg, Germany
†Current address: Diamond Light Source Ltd, Harwell Science and Innovation Campus, Didcot OX11 0DE, UK
*e-mail: j.a.vanbokhoven@chem.ethz.ch; tien-lin.lee@diamond.ac.uk

Published online: 22 June 2008; doi:10.1038/nmat2220

Zeolites are microporous crystalline materials that find wide application in industry, for example, as catalysts and gas separators, and in our daily life, for example, as adsorbents or as ion exchangers in laundry detergents[1]. The tetrahedrally coordinated silicon and aluminium atoms in the zeolite unit cell occupy the so-called crystallographic T-sites. Besides their pore size, the occupation of specific T-sites by the aluminium atoms determines the performance of the zeolites[2]. Despite its importance, the distribution of aluminium over the crystallographic T-sites remains one of the most challenging, unresolved issues in zeolite science. Here, we report how to determine unambiguously and directly the distribution of aluminium in zeolites by means of the X-ray standing wave technique[3] using brilliant, focused X-rays from a third-generation synchrotron source. We report in detail the analysis of the aluminium distribution in scolecite, which demonstrates how the aluminium occupancy in zeolites can systematically be determined.

Zeolites are widely used materials with a very wide range of applications. They are used in households in laundry detergents and in industry as catalysts for petrochemical refining and they have become increasingly important in fine-chemical production and in environmental applications; they are used as air and water purifiers and in heating and refrigerating, and they are used in agriculture as selective absorbents. With natural zeolites being discovered more than 200 years ago, intensive research is nowadays aimed at developing new, synthetic zeolites with tailored properties for specific tasks. The functionality of a zeolite is determined basically by just a few parameters: the size and connectivity of the pores and cages, the Si/Al ratio and the placement of the trivalent aluminium atoms at specific crystallographic T-sites. Among them, the placement of aluminium is still unknown for many zeolites because no generally applicable experimental method has been reported to solve this problem. This seriously hampers the understanding of the function of some technologically important zeolites and hinders the development of new zeolites with novel functionalities.

In a zeolite, the replacement of a tetravalent silicon atom by a trivalent aluminium atom on a T-site places a negative charge on the framework, which is compensated by non-framework cations. These charge-compensating cations are loosely held in the pores and cages of a zeolite and can be exchanged by other cations. This property makes zeolites good cation exchangers, which are useful in water softening and in the removal of nuclear waste. When the charge-compensating species are protons or elements that are involved in oxidation or reduction reactions, zeolites become catalytically active in Brønsted and redox reactions, respectively. The Si/Al ratio and the aluminium distribution over the framework T-sites thus determine the species and the positions of the charge-compensating cations in a zeolite, which strongly affect its catalytic performance and chemical functionality[1,4,5]. Also closely related to the aluminium occupation is the stability of zeolites. It has been shown that destruction of the framework by dealumination of zeolites depends on the distribution of aluminium over the T-sites[6] as well. Variation in synthesis parameters affects the distribution of aluminium over the T-sites[7].

By combining the results of many different experimental methods[8–10], the zeolite structure database[2] was established. Some insight into the aluminium distribution was obtained by NMR and neutron diffraction and by replacing aluminium with atoms such as Ti, Fe, Ga and B (refs 11–16). However, discriminating between aluminium and silicon on the T-sites remained impossible in many cases. Thus, an unambiguous assignment of aluminium and silicon to the T-sites is therefore still lacking, although the atomic coordinates of the T-sites have been accurately determined by structure refinement based on diffraction data.

To directly determine the aluminium occupation of T-sites in zeolites, we use the X-ray standing wave (XSW) technique and present here, as an example, the analysis of the well-known zeolite scolecite. It belongs to the natrolite structure type with a composition $|Ca_4(H_2O)_{12}|[Si_{12}Al_8O_{40}]$, where the calcium acts as the charge-compensating cation. Figure 1 shows the building units and the atomic structure of scolecite based on a previous refinement using neutron and X-ray diffraction data[17]. Our sample

was a natural crystal of scolecite (Fig. 2b) and originated from Pune, India. The Si/Al atomic ratio was determined by energy-dispersive X-ray spectroscopy as 3:2.

The XSW method is able to determine the amplitudes and phases of the Fourier components of a distribution of atoms within a crystal lattice[18]. By recording the characteristic X-ray fluorescence or photoelectrons from a sample under the influence of the standing wave (Fig. 2c), the method becomes element specific and chemically sensitive[3]. This enables analysis of the site distribution of all framework and extra-framework elements in zeolite materials simultaneously and independently.

Three virtually orthogonal reflections, (040), (002) and ($\bar{4}02$) (Fig. 1b,c), with a lattice spacing of 0.474, 0.462 and 0.163 nm, respectively, were used for the XSW measurements, which were carried out at the insertion device beamline ID32 at the European Synchrotron Radiation Facility in Grenoble, France. Figure 2a shows a schematic diagram of the experimental set-up with the inset illustrating the principle of XSW.

Figure 2c shows an X-ray fluorescence spectrum measured from the scolecite crystal. Such a spectrum was recorded and the peak intensities of the Al K, Si K and Ca Kα X-ray fluorescence were integrated at each step of the XSW scans traversing the three Bragg reflections. Figure 3 shows these integrated and normalized fluorescence yields versus the angle of the incident beam, θ. The distinctly different modulations observed in the yield curves for aluminium and silicon show already unambiguously that both elements are distributed dissimilarly over the crystallographic T-sites.

The normalized fluorescence yield excited by an XSW field can be described by[19,20]

$$Y_{\mathrm{H}}(\theta) = \left\{1 + R_{\mathrm{H}}(\theta) + 2\sqrt{R_{\mathrm{H}}(\theta)} f_{\mathrm{H}} \cos(\nu_{\mathrm{H}}(\theta) - 2\pi P_{\mathrm{H}})\right\} L_{\mathrm{H}}(\theta), \quad (1)$$

where $R_{\mathrm{H}}(\theta)$ is the reflectivity and $L_{\mathrm{H}}(\theta)$ is the effective depth of the sample from which the fluorescence is observed. The phase of the XSW, $\nu_{\mathrm{H}}(\theta)$, changes by π over the angular range of the Bragg reflection. In equation (1), $R_{\mathrm{H}}(\theta)$, $\nu_{\mathrm{H}}(\theta)$ and $L_{\mathrm{H}}(\theta)$ can be calculated from the dynamical theory of X-ray diffraction and known experimental parameters[21,22]. The fitting parameters f_{H} and P_{H} (see below), commonly referred to as the coherent fraction and coherent position, respectively, represent the result of an XSW measurement.

For atoms of the same element occupying M positions ($\mathbf{r}_j$) within the unit cell, the Fourier component G_{H} for a reflection $\mathbf{H}$ is given by[17,20]

$$G_{\mathrm{H}} = \left(\frac{D_{\mathrm{H}}}{N}\right) \sum_{j=1}^{M} C_j \exp(2\pi i \mathbf{H} \cdot \mathbf{r}_j) = D_{\mathrm{H}} a_{\mathrm{H}} \exp(2\pi i P_{\mathrm{H}}), \quad (2)$$

where D_{H} is the Debye–Waller factor, accounting for the broadening of the atomic distribution due to thermal vibration and static disorder of the lattice, C_j is the probability of the position $\mathbf{r}_j$ being occupied by the element with $N = \sum C_j$ and a_{H} is the geometric factor describing the distribution over different sites $\mathbf{r}_j$. One XSW measurement determines the amplitude, $f_{\mathrm{H}} = D_{\mathrm{H}} a_{\mathrm{H}}$ ($0 \le f_{\mathrm{H}} \le 1$), and phase, P_{H} ($0 \le P_{\mathrm{H}} \le 1$), of G_{H}.

Using equation (2) and the atomic coordinates in ref. 17, we calculated a_{H} and P_{H} for the scolecite (040), (002) and ($\bar{4}02$) reflections. We allowed silicon and aluminium to occupy any of the T-sites by introducing aluminium occupancy factors ($C_a = C_b = C_{ab}$, $C_c = C_d = C_{cd}$ for a, b, c and d of the T_1-sites and C_{T_2} for the T_2-site in Fig. 1b,c) with the boundary condition that the overall Si/Al atomic ratio is 3:2. The analysis also included Debye–Waller factors, D_{Al}, D_{Si} and D_{Ca}, to account for some atomic distribution around the basic structure. For each reflection, $R_{\mathrm{H}}(\theta)$, $\nu_{\mathrm{H}}(\theta)$ and $L_{\mathrm{H}}(\theta)$ were calculated and C_{ab}, C_{cd}, D_{Al}, D_{Si} and D_{Ca} were varied until the best agreement between the measured and

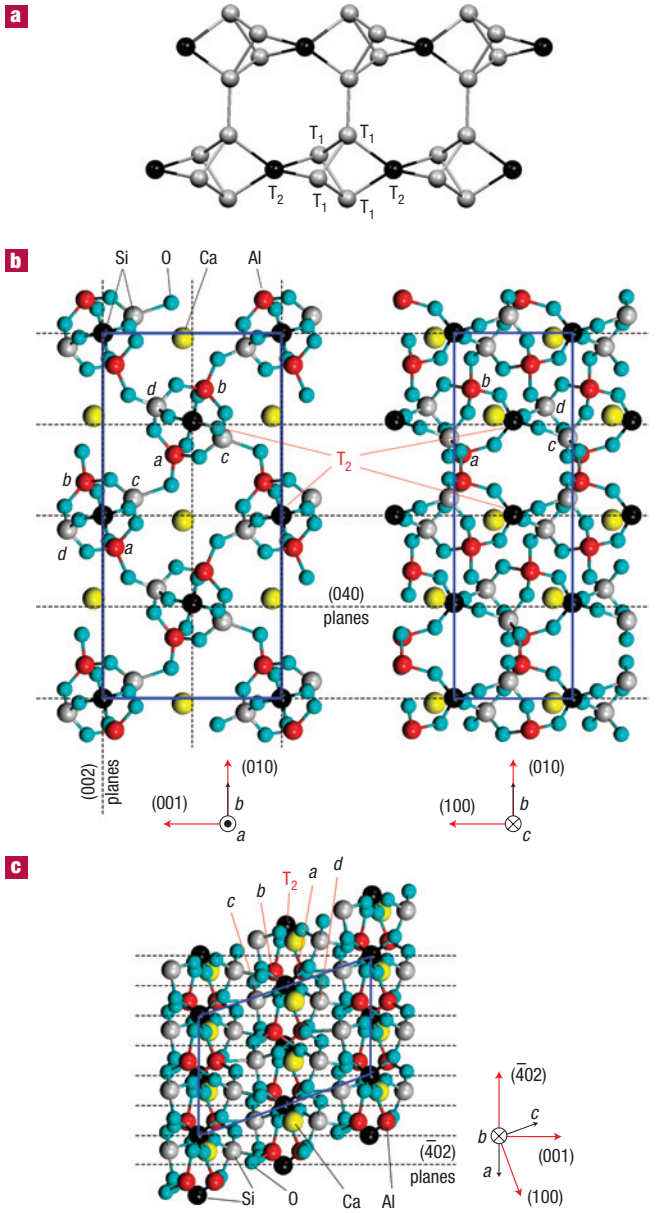

Figure 1 Structure of scolecite. a, Six of the secondary building units (SBUs) of scolecite, which form natrolite chains. The spheres represent the crystallographic T-sites that are occupied by aluminium or silicon and the sticks represent the oxygen atoms that bridge the T-sites. Each SBU is composed of five T-atoms, four T_1-atoms and one T_2-atom. The T_2-atom links two adjacent SBUs along the chain, whereas larger pores are formed by bridging oxygen atoms that connect the T_1-atoms of neighbouring chains. In scolecite, the chains are parallel to the crystallographic *a* axis. **b**,**c**, Projections of the atomic structure of scolecite[17] along the three axes of the unit cell, which is marked by the blue rectangles and paralellogram. The monoclinic unit cell has lattice parameters of $a = 0.6522$ nm, $b = 1.8968$ nm, $c = 0.9840$ nm, $\alpha = \gamma = 90^\circ$ and $\beta = 109.97^\circ$. There are 20 T-sites per unit cell. The four T_1-sites associated with each T_2-site are labelled *a*, *b*, *c* and *d*. The dashed lines denote the Bragg planes where $P = 0$ for the scolecite (040), (002) and ($\bar{4}02$) reflections.

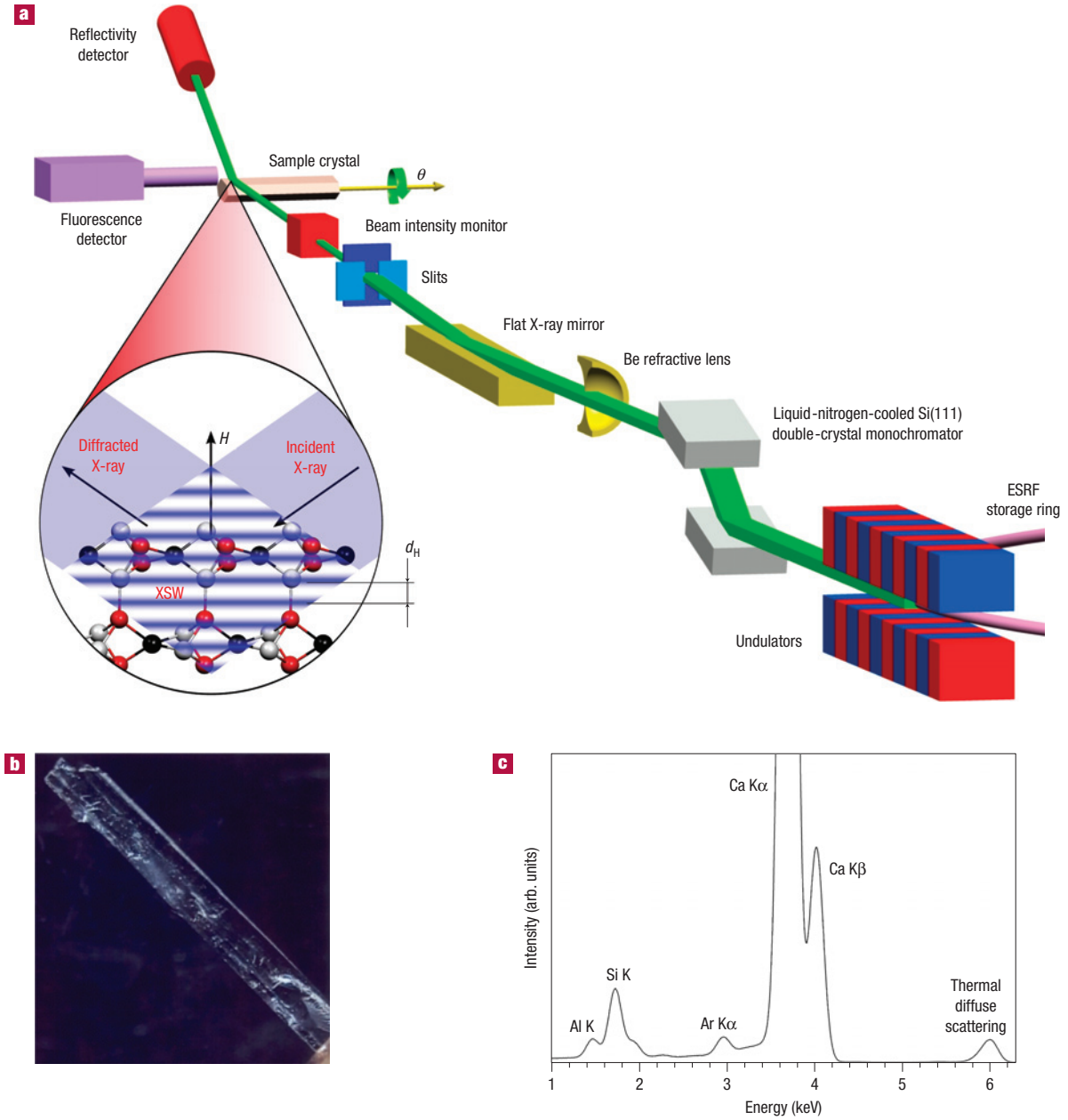

Figure 2 Experimental details. a, Schematic diagram of the set-up for the synchrotron XSW experiment. Inset: Illustration of the principle of the XSW method: an X-ray standing wave in the natrolite structure. **b**, Image of the scolecite crystal used in this experiment. The crystal was about 500–800 μm in diameter and 5 mm in length. The crystallographic (*a*) axis is parallel to the long axis of the crystal. Around this axis, six facets, parallel to the (010), (011) or (01$\bar{1}$) atomic planes, form the surfaces of the crystal. **c**, Fluorescence spectrum measured from the scolecite crystal with incident X-rays of 6.00 keV.

calculated (equation (1)) fluorescence yields of all three elements was achieved. As the calcium atoms occupy a single site, only the corresponding Debye–Waller factor was varied during the fitting procedure. The best fits to the fluorescence data are plotted as red curves in Fig. 3 and the thus-determined aluminium occupancy factors are listed in Table 1.

Figure 3 shows that all of the measured fluorescence yields are well reproduced by the calculated ones based on the best fit of the occupation (and the known atomic coordinates). The values of $C_{ab} = 1$ and $C_{cd} = 0$ for all three reflections in Table 1 reveal unambiguously that aluminium is positioned only at *a* and *b* of the T_1-sites. To illustrate the sensitivity of the XSW method, we plotted in Fig. 3 simulated Al and Si Kα fluorescence modulations (blue and green lines) of the three reflections assuming mixed occupations of the T-sites by silicon and aluminium. The modulations of the simulated curves are clearly distinguishable from the measured ones, demonstrating that XSW can detect the lattice site of small fractions of aluminium.

We have also carried out a similar experimental XSW study on mesolite. Furthermore, to investigate the applicability of the XSW technique to other zeolites with unknown and more complex aluminium site distributions, we chose as an example ZSM-5, a

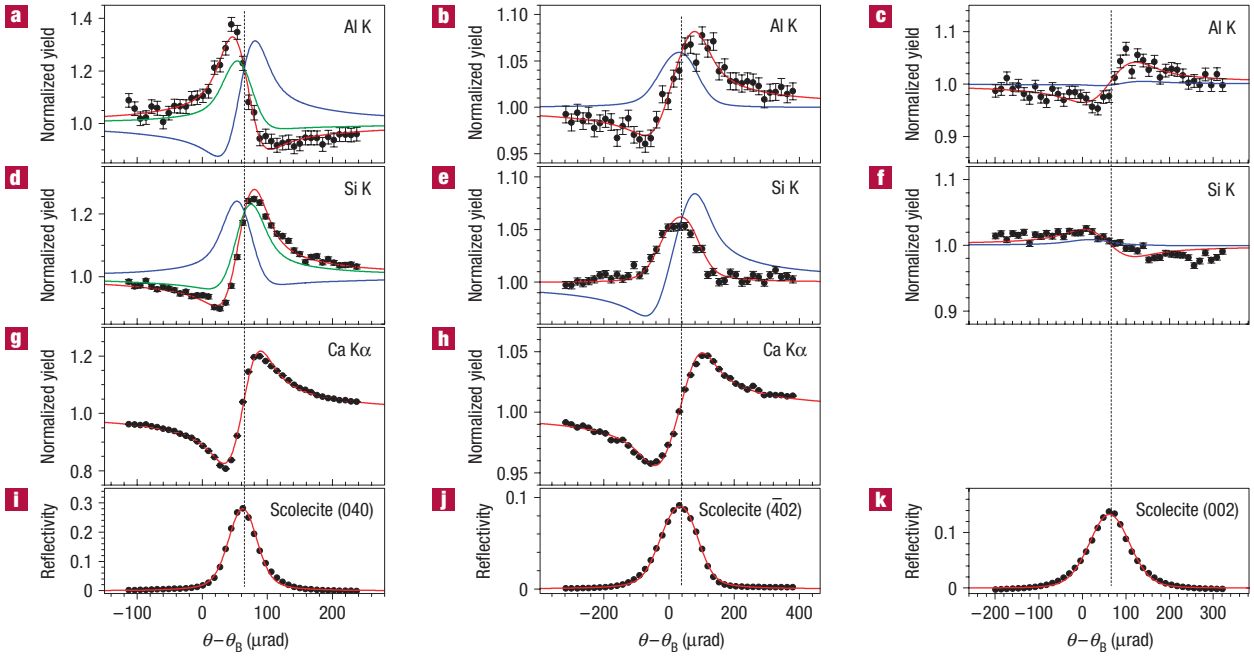

Figure 3 Experimental results on scolecite. a–k, The XSW-induced Al K, Si K and Ca Kα fluorescence yields, normalized to the yield measured away from the Bragg reflection, Y_{H0} (filled circles in **a–h**), and the measured reflectivity (filled circles in **i–k**) obtained from θ scans of the (040), ($\bar{4}02$) and (002) reflections. The red curves are the best fits to the data, which determine the occupancy factors listed in Table 1. The blue and green curves represent the simulated yields assuming different occupation of the T-sites keeping the Si/Al ratio at 3:2. Blue curves: aluminium occupancy factors $C_{ab} = 0$, $C_{cd} = 0.5$ and $C_{T_2} = 1.0$. Green curves: $C_{ab} = 0.7$, $C_{cd} = 0.15$ and $C_{T_2} = 0.3$. In both cases, the remaining T-sites are assigned to silicon.

Table 1 Aluminium occupancy factors (C_{ab}, C_{cd} and C_{T_2}) deduced from the XSW analysis for the scolecite (040), ($\bar{4}02$) and (002) reflections. The error in the occupancy values is estimated to be 0.06.

	(040)	($\bar{4}02$)	(002)
C_{ab}	1	1	1
C_{cd}	0	0	0
C_{T_2}	0	0	0

zeolite that is widely used as a shape-selective catalyst in industrial hydrocarbon conversion. The framework of ZSM-5 had been determined previously by X-ray diffraction[23] and contains 12 non-equivalent T-sites, each occupied by 8 Si/Al atoms per unit cell. The structure is one of the most complex ones. Compared with the analysis of scolecite, collecting more Fourier components (G_H) is mandatory to resolve the larger number of T-sites in ZSM-5. In this way, the direct reconstruction of the distributions of aluminium from the G_H values through Fourier expansions is possible. Our analysis (see the Supplementary Information) shows that, even with a moderate number of Fourier components being measured, the XSW method is capable of identifying the different T-sites occupied by aluminium in ZSM-5 by virtue of the phase-sensitive and element-specific nature of the technique. However, to carry out such an experimental study will require improvements in beamline instrumentation, which are currently under way.

In summary, with the help of the chemical sensitivity and real-space resolution of the XSW technique, we find that aluminium in scolecite is highly ordered and we identified unambiguously and with high accuracy the specifically occupied crystallographic T-sites. The measurements were possible by using focused synchrotron X-rays, illuminating a small grain of millimetre-sized crystals of natural origin. Zeolites that are industrially applied or are synthesized in the laboratory have much smaller crystal sizes, often not larger than a few micrometres. However, XSW measurements with microscopic resolution are feasible[24]. With more highly brilliant synchrotron X-ray sources, further development of X-ray microfocusing optics, better detectors and higher accuracy diffractometers for XSW measurements on micrometre-sized samples, we expect that the XSW technique can routinely be applied to such small zeolite crystals and other complex materials.

METHODS

A second X-ray wavefield is produced when a plane X-wave is Bragg diffracted by a highly perfect single crystal. The interference of the diffracted X-ray beam with the incident beam gives rise to an XSW (Fig. 2a, inset). Under the Bragg diffraction condition for a reflection **H**, the phase of the XSW ($\nu_H(\theta)$ in equation (2)) varies with the incident angle (θ). Thus, by changing θ, we can move the nodes and antinodes of the XSW, which have a periodicity identical to the Bragg plane spacing d_H, along the **H** direction within half of d_H. This movement of the XSW adds to the secondary emissions, such as X-ray fluorescence and photoelectrons of an element in the wavefield, an intensity modulation that is characteristic of its crystallographic position. By measuring and analysing such a modulation induced by XSW, we can determine the site or spatial distribution of the element with respect to the Bragg planes of reflection **H**. The dashed lines in Fig. 1b,c indicate the corresponding Bragg planes where $P_H = 0$ for the scolecite (040), (002) and ($\bar{4}02$) reflections.

The X-rays were emitted from the 6 GeV electron beam of the ESRF passing through an undulator with a period of magnetic field of 35 mm. Photons with an energy of 6.00 keV were selected by a pair of liquid-nitrogen-cooled Si(111) monochromator crystals (Fig. 2a). The monochromatic beam was focused by a beryllium refractive lens about 15 m before the sample and then deflected by a flat mirror for rejecting the high-order harmonics, resulting in a beam size of 30 (V) × 350 (H) μm^2 at the slits, which reduced the beam

size further to 20 $(V) \times 100$ (H) μm^2 at the sample. To generate XSWs, the sample crystal was mounted on a six-circle diffractometer and oriented to excite the chosen Bragg reflections. The small beam was necessary because only a part of the mosaic sample crystal was found to exhibit sufficient crystalline quality. For each XSW measurement, we monitored simultaneously the intensity of the diffracted X-rays and the fluorescence signals emitted from the crystal, while scanning θ through the reflection. To account for some crystalline imperfections, each calculated $R_H(\theta)$ (equation (1)) was broadened by a gaussian function. To minimize the effect of secondary extinction, thus avoiding large variations of $L_H(\theta)$ (equation (1)) and keeping it close to unity, the fluorescence was detected at a small exit angle with the sample surface, whenever possible.

Received 22 October 2007; accepted 19 May 2008; published 22 June 2008.

References

1. Maxwell, I. E. & Stork, W. H. J. Hydrocarbon processing with zeolites. *Stud. Surf. Sci. Catal.* **137**, 747–819 (2001).
2. Baerlocher, C., Meier, W. M. & Olson, D. H. *Atlas of Zeolite Framework Types* 5th revised edn (Elsevier, Amsterdam, 2001) <http://topaz.ethz.ch/IZA-SC/StdAtlas.htm>.
3. Cheng, L., Fenter, P., Bedzyk, M. J. & Sturchio, N. C. Fourier-expansion solution of atom distributions in a crystal using x-ray standing waves. *Phys. Rev. Lett.* **90**, 255503 (2003).
4. Armbruster, T. Clinoptilolite-heulandite: Applications and basic research. *Stud. Surf. Sci. Catal.* **135**, 13–27 (2001).
5. Dedecek, J., Kaucky, D., Wichterlova, B. & Gonsiorova, O. Co^{2+} ions as probes of Al distribution in the framework of zeolites. ZSM-5 study. *Phys. Chem. Chem. Phys.* **4**, 5406–5413 (2002).
6. van Bokhoven, J. A., Koningsberger, D. C., Kunkeler, P., van Bekkum, H. & Kentgens, A. P. M. Stepwise dealumination of zeolite beta at specific T-sites observed with ^{27}Al MAS and ^{27}Al MQ MAS NMR. *J. Am. Chem. Soc.* **112**, 12842–12847 (2000).
7. Sklenak, S. *et al.* Aluminum siting in silicon-rich zeolite frameworks: A combined high-resolution ^{27}Al NMR spectroscopy and quantum mechanics/molecular mechanics study of ZSM-5. *Angew. Chem. Int. Ed.* **46**, 7286–7289 (2007).
8. Kokotailo, G. T., Lawton, S. L., Olson, D. H. & Meier, W. M. Structure of synthetic zeolite ZSM-5. *Nature* **272**, 437–438 (1978).
9. Treacy, M. M. J. & Newsam, J. M. Two new three-dimensional twelve-ring zeolite frameworks of which zeolite beta is a disordered intergrowth. *Nature* **332**, 249–251 (1988).
10. Fyfe, C. A., Gobbi, G. C., Klinowski, J., Thomas, J. M. & Ramdas, S. Resolving crystallographically distinct tetrahedral sites in silicalite and ZSM-5 by solid-state NMR. *Nature* **296**, 530–533 (1982).
11. Henry, P. F., Weller, M. T. & Wilson, C. C. Structural investigation of TS-1: Determination of the true nonrandom titanium framework substitution and silicon vacancy distribution from powder neutron diffraction studies using isotopes. *J. Phys. Chem. B.* **105**, 7452–7458 (2001).
12. Hijar, C. A. *et al.* The siting of Ti in TS-1 is non-random. Powder neutron diffraction studies and theoretical calculations of TS-1 and FeS-1. *J. Phys. Chem. B* **104**, 12157–12164 (2000).
13. Lamberti, C. *et al.* Ti location in the MFI framework of Ti-silicalite-1: A neutron powder diffraction study. *J. Am. Chem. Soc.* **123**, 2204–2212 (2001).
14. Marra, G. L., Artioli, G., Fitch, A. N., Milanesio, M. & Lamberti, C. Orthorhombic to monoclinic phase transition in high-Ti-loaded TS-1: An attempt to locate Ti in the MFI framework by low temperature XRD. *Microporous Mesoporous Mater.* **40**, 85 (2000).
15. Milanesio, M. *et al.* Iron location in Fe-silicalites by synchrotron radiation single crystal x-ray diffraction. *J. Phys. Chem. B* **104**, 9951–9953 (2000).
16. Palin, L., C. *et al.* Single-crystal synchrotron radiation x-ray diffraction study of B and Ga silicalites compared to a purely siliceous MFI: A discussion of the heteroatom distribution. *J. Phys. Chem. B* **107**, 4034–4042 (2003).
17. Smith, J. V., Pluth, J. J., Artioli, G. & Ross, F. K. in *Proc. 6th Int. Zeolite Conf.* (eds Olson, D. & Bisio, A.) 842–850 (Buttersworth, London, 1984).
18. Hertel, N., Materlik, G. & Zegenhagen, J. X-ray standing wave analysis of bismuth implanted in Si(110). *Z. Phys. B* **58**, 199–204 (1985).
19. Zegenhagen, J. Surface-structure determination with x-ray standing waves. *Surf. Sci. Rep.* **18**, 199–271 (1993).
20. Lee, T. -L. *et al.* The use of x-ray standing waves and evanescent-wave emission to study buried strained-layer heterostructures. *Physica B* **221**, 437–444 (1996).
21. Batterman, B. W. Effect of dynamical diffraction in x-ray fluorescence scattering. *Phys. Rev.* **133**, A759 (1964).
22. Zegenhagen, J., Materlik, G. & Uelhoff, W. X-ray standing wave analysis of highly perfect Cu crystals and electrodeposited submonolayers of Cd and Tl on Cu surfaces. *J. X-ray Sci. Tech.* **2**, 214–239 (1990).
23. van Koningsveld, H., van Bekkum, H. & Jansen, J. C. On the location and disorder of the tetrapropylammonium (TPA) ion in zeolite ZSM-5 with improved framework accuracy. *Acta Crystallogr., B* **43**, 127–132 (1987).
24. Drakopoulos, M. *et al.* X-ray standing wave microscopy: Chemical microanalysis with atomic resolution. *Appl. Phys. Lett.* **81**, 2279–2281 (2002).

Supplementary Information accompanies this paper on www.nature.com/naturematerials.

Acknowledgements

We thank the staff of the ESRF and the ID32 beamline, in particular L. Andre and H. Isern, for skillful technical assistance. Financial support by a grant (05 KS4GU3/4) to S.T. from the German Federal Ministry for Education and Research (BMBF) is gratefully acknowledged. Financial support from the Swiss National Science Foundation (PP002–110473) to J.A.v.B. is also gratefully acknowledged. We thank L. McCusker for careful reading of the manuscript.

Author information

Reprints and permission information is available online at http://npg.nature.com/reprintsandpermissions. Correspondence and requests for materials should be addressed to J.A.v.B. or T.-L.L.